

# GG Tauri: the ring world

S. Guilloteau<sup>1</sup>, A. Dutrey<sup>1</sup>, and M. Simon<sup>2</sup>

<sup>1</sup> Institut de Radio Astronomie Millimétrique, 300 Rue de la Piscine, F-38406 Saint Martin d'Hères, France

<sup>2</sup> Department of Physics and Astronomy, State University of New York, Stony Brook, NY 11794-3800, USA

Received 22 October 1998 / Accepted 16 April 1999

**Abstract.** We present sub-arcsecond images of the mm dust emission and  $^{13}\text{CO}$  J=2–1 line emission in the young quadruple system GG Tau. These observations unambiguously resolve the circumbinary disk of the close ( $\sim 0.3''$ ) binary system into two distinct components: an extremely dense, sharp-edged ring, surrounded by an extended disk. Continuum emission is also detected from the center of this structure; it probably arises in the small circumstellar disk or disks of the binary. The kinematic data show that the ring+disk system is in Keplerian rotation and yield the estimate  $M = (1.28 \pm 0.07)(D/140 \text{ pc})M_{\odot}$  for the mass of the binary stars. We derive the physical parameters of the ring and disk from these data and from new  $2''$  resolution images of the  $\text{HCO}^+$  J=1–0 line and 3.4 mm continuum emission. The temperature in the ring + disk system is consistent with heating by the stellar light (including the IR excess coming from the inner disks). Comparison with the optical/NIR images indicates a disk thickness compatible with an hydrostatic equilibrium.

**Key words:** stars: binaries: close – stars: circumstellar matter – stars: individual: GG Tau – stars: pre-main sequence – radio continuum: stars – radio lines: stars

## 1. Introduction

GG Tau has become invaluable for our understanding of young star binaries and their associated disks. It is a quadruple, consisting of a close,  $\sim 0.3''$ , binary, and  $\sim 10''$  to the south, a second binary with  $\sim 1.4''$  separation (Leinert et al. 1993). Most of the results described here pertain to the northern, close binary. We adopt the distance 140 pc (Elias 1978); at this distance, the components of the close binary, GG Tau A and GG Tau a, are separated by  $\sim 45$  AU (we adopt the designation given by Roddier et al. 1996, hereafter RRNGJ). The unresolved system is classified as a classic emission line T Tauri (Herbig & Bell 1988). The standard model of T Tauri activity powered by accretion implies therefore that at least one of the stars is associated with an active circumstellar disk. The binary is surrounded by a disk resolved in its CO and dust emission and near infrared scattered light (Dutrey et al. 1994, DGS94; RRNGJ). Estimates

of the total stellar mass derived from the Keplerian rotation of the circumbinary disk and the orbital motion of stars lie in the range 1.0–1.6  $M_{\odot}$  (DGS94, RRNGJ). Mm-wave detections of diverse molecules in the circumbinary disk provide estimates of the  $\text{H}_2$  densities required for excitation of their spectral lines, demonstrate that the molecules are underabundant relative to molecular clouds, and enable the study of gas phase chemistry under conditions very different from that in the molecular clouds (Dutrey et al. 1997, DGG97).

We have obtained new interferometric observations of the system in the  $^{13}\text{CO}$  J=2–1 line and continuum at 1.4 mm and the  $\text{H}^{12}\text{CO}^+$  J=1–0 line at 3.4 mm. The 1.4 mm wavelength observations reach a resolution  $\sim 3$  times greater than that in DGS94 and reveal for the first time distinct and angularly resolved regions of the dust and line emissions. The  $\text{H}^{12}\text{CO}^+$  emission is detected mostly from the outer regions of the disk. We describe our results here.

## 2. Observations and data reduction

Data were taken with the IRAM Plateau de Bure Interferometer (Guilloteau et al. 1992) between Jan 1997 and Apr 1997. We used the dual frequency system to observe simultaneously the  $\text{HCO}^+$  J=1–0 line, 3.4 mm continuum,  $^{13}\text{CO}$  J=2–1 line and 1.4 mm continuum. At 3.4 mm, the receivers, tuned single-sideband, offered typical SSB system temperature around 130 K. One correlator unit of bandwidth 160 MHz was used for the continuum, while a narrow band 8 MHz unit was used to provide 160 channels of 39 kHz separation for  $\text{HCO}^+$  J=1–0 (effective resolution 60 kHz, or  $0.20 \text{ km s}^{-1}$ ). At 1.4 mm, the receivers were tuned double sideband, with a typical SSB system temperature around 300 K. 3 correlator units were used to provide a continuum bandwidth of 500 MHz, while the  $^{13}\text{CO}$  J=2–1 line was observed using a 20 MHz bandwidth with 256 channels (channel separation 79 kHz, effective resolution 120 kHz or  $0.16 \text{ km s}^{-1}$ ). Baselines ranging between 24 m and 408 m provided an angular resolution of  $0.85 \times 0.60''$  at 1.4 mm, and  $2.4 \times 1.7''$  at 3.4 mm (at position angle  $14^\circ$ ). Phase and amplitude calibrations were performed using 0415+379 and 0528+134, whose flux is regularly monitored against planets. Excellent weather conditions prevailed during the observations, with phase noise less than  $30^\circ$  at 1.4 mm even on the

*Send offprint requests to:* S. Guilloteau

*Correspondence to:* guillote@iram.fr

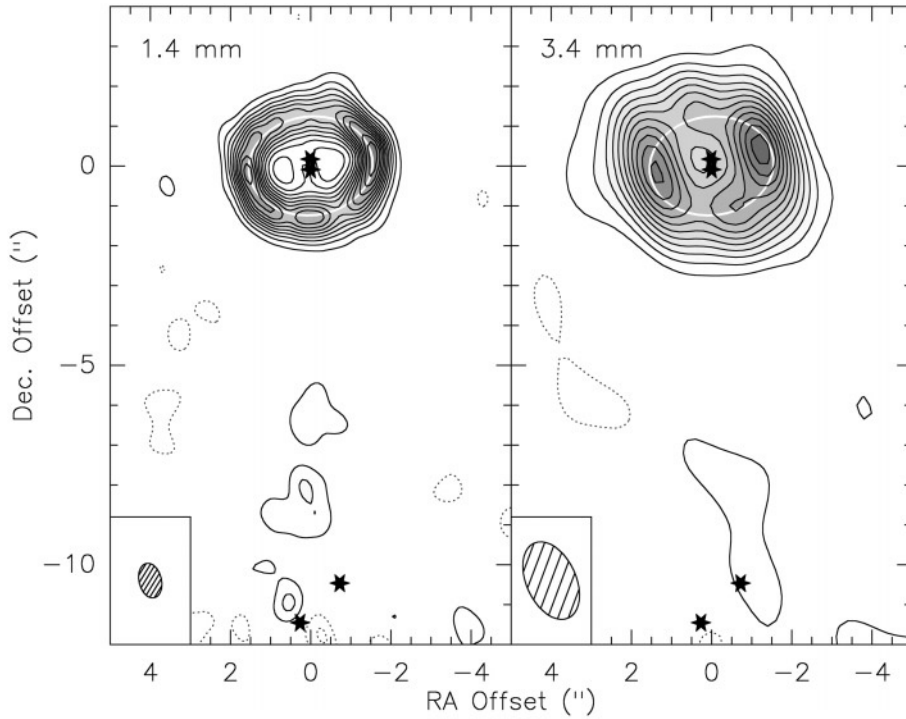


**Fig. 1.** *Left:* 1.4 mm wavelength continuum map of GG Tau. The synthesized beam is  $0.88 \times 0.56''$  at PA  $13^\circ$ . The contour levels are multiples of the step of 4 mJy/beam (zero level is omitted). Correction for primary beam attenuation has been applied, resulting in increasing noise level near the wider binary GG Tau B/b. *Right:* 3.4 mm wavelength continuum map. The synthesized beam is  $2.06 \times 1.24''$  at PA  $24^\circ$ . Contour levels are in step of 0.7 mJy. The small black stars indicates the positions of the stars. The white ellipse is the projection of a circle of  $1.55''$  radius, inclined at  $37^\circ$  from the plane of the sky, at a position angle of  $7^\circ$ . Coordinates are offset from R.A.  $04^{\text{h}}32^{\text{m}}30.342^{\text{s}}$  Declination  $17^\circ31'40.52''$  (J2000.0). The position accuracy is about  $0.05''$

longest baselines. The effective seeing, estimated by calibrating 0415+379 against 0528+134, is about  $0.2''$ , and the absolute astrometry is better than  $0.05''$ .

Image processing and cleaning were done in the standard way using the GILDAS software. For simplicity, the  $^{13}\text{CO}$  and  $\text{HCO}^+$  data were resampled to provide  $0.25 \text{ km s}^{-1}$  resolution, and in addition, the  $\text{HCO}^+$  J=1–0 line was restored with a circular beam of  $2''$ .

### 3. Observational results

#### 3.1. Structure of the continuum

The total continuum flux density we measure at 1.4 mm is  $570 \pm 20$  mJy, in excellent agreement with the Beckwith et al. (1990) value. Fig. 1 shows its distribution seen with our synthesized beam of  $0.9 \times 0.6''$ . For the first time, we resolve emission from inside the circumbinary disk; about 10 mJy is centered at the position of the binary stars and probably arises in their circumstellar disk or disks. The remainder,  $> 95\%$  of the continuum flux, originates in circumbinary material. Fig. 1 shows that most of this,  $510 \pm 10$  mJy, is radiated by a ring in the innermost part of the circumbinary disk (see also Fig. 2), while some emission ( $60 \pm 20$  mJy after correction for primary beam attenuation) surrounds it or may be located between GG Tau A/a and the second binary, GG Tau B/b.

We modeled the observed  $u, v$ -plane visibilities to make this statement more quantitative. A model in which 90% of the circumbinary emission arises in a ring located between radii  $1.27$  and  $1.90'' (\pm 0.01)$  and the rest in a disk extending to  $\sim 4''$  radius, both tilted at inclination  $i = 37^\circ \pm 1$  and lying at PA  $7^\circ \pm 2$ , provides an excellent fit to the observed visibilities

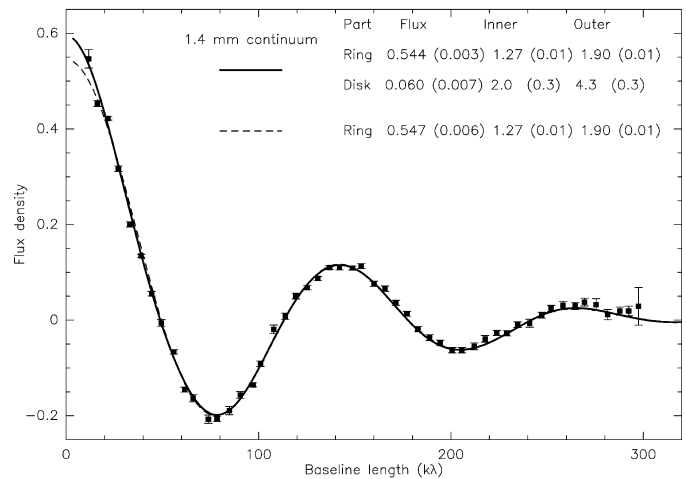


**Fig. 2.** 1.4 mm continuum  $uv$  plane visibility, plotted as the real part of the flux, as a function of circularised baseline length (in units of the wavelength) for the observed data (solid dots and  $\pm 1\sigma$  error bars), and the ring plus extended disk (thick line) and ring only models (dashed line) described in Sect. 3.1. The  $uv$  coordinates were rotated and stretched along the  $v$  axis by  $\cos(37^\circ)$  to compensate for the inclination of the disk.

(Fig. 2). To demonstrate the evidence in our data for weak but extended continuum emission, Fig. 2 also shows the visibility function calculated for a model consisting only of a ring with geometry as above. This model clearly fits less well, particularly at the short baseline spacings. With a width of  $\sim 0.6''$ , our observations just resolve the ring.

The continuum map also shows that the continuum emission of the ring appears slightly asymmetric, with the Western part

**Table 1.** Size and Flux density measurements for GG Tau

	Part	Integrated Flux	Inner radius (")	Outer radius (")	Ref.
3.4 mm	Ring+Disk	38 ± 2 mJy	-	-	This work
2.7 mm	Ring+Disk	85 ± 5 mJy	-	-	DGS94
1.4 mm	Ring	544 ± 3 mJy	1.27 ± 0.01	1.90 ± 0.01	This work
	Disk	60 ± 7 mJy	2.00 ± 0.30	4.30 ± 0.30	-
1.3 mm	Ring+Disk	593 ± 53 mJy	Unresolved	Unresolved	Beckwith et al. 1990
<sup>13</sup> CO	Ring	5.20 ± 0.20 Jy.km s <sup>-1</sup>	1.10 ± 0.06	1.90*	This work
	Disk	3.20 ± 0.24 Jy.km s <sup>-1</sup>	1.90*	3.28 ± 0.16	-
HCO <sup>+</sup>	Ring	0.44 ± 0.03 Jy.km s <sup>-1</sup>	1.25*	1.90*	This work
	Disk	0.51 ± 0.03 Jy.km s <sup>-1</sup>	1.90*	3.60 ± 0.15	-

\* indicates a fixed parameter.

somewhat brighter than the Eastern part. The effect is more pronounced in the 3.4 mm map, was also observed in the 2.7 mm map from DGS94. We caution however that the apparent clumpy structure of the ring in the 1.4 mm continuum image is not significant. If a uniform ring model is removed from the observed 1.4 mm data, the residual image does not show any obvious feature (at the ring location).

### 3.2. The <sup>13</sup>CO and HCO<sup>+</sup> line emission

The velocity channel maps of <sup>13</sup>CO J=2–1 emission (Fig. 3) show that the emission is resolved. The <sup>13</sup>CO emission peaks at the position of the bright ring delineated by the dust continuum emission, and extends to the outer regions of the circumbinary disk. The strength of the <sup>13</sup>CO signal at large radii demonstrates the technical point that <sup>13</sup>CO is a better tracer of material in outer disks than dust (e.g., Sect. 4.1 in Dutrey et al. 1996). The progression from blue-shifted emission in the east to red-shifted in the west seen in the velocity channel maps and the velocity gradient map confirms the interpretation of Keplerian rotation of the circumbinary disk by DGS94. We model its kinematics in Sect. 4.2 and use the best-fitting model to derive an independent estimate of the disk orientation relative to our line of sight.

Since the line must be optically thick and thermalized in the ring because the H<sub>2</sub> gas density is high (see below and Sect. 4.2), the observed brightness temperature measures the gas kinetic temperature,  $T_k$ , after correction for beam dilution. For a ring of 0.6" width and 1.5" radius observed with a  $0.9 \times 0.6''$  beam, the beam filling factor is about 0.7. Hence the peak intensity  $\sim 350$  mJy/beam at the bright ring therefore indicates  $T_k \sim 35$  K.

Fig. 4 shows the distribution of HCO<sup>+</sup> J=1–0 emission. Although the angular resolution of this observation is lower than that of <sup>13</sup>CO, the maps resolve the HCO<sup>+</sup> emission and convey the same sense of rotation of a tilted disk. The peak intensity  $\sim 130$  mJy/beam at  $v = 5.4$  and  $7.2$  km s<sup>-1</sup> corresponds to brightness temperature  $\sim 5$  K indicating that the HCO<sup>+</sup> emission is optically thin. The J=1–0 HCO<sup>+</sup> line requires  $n(\text{H}_2) > 6 \times 10^4$  cm<sup>-3</sup> for collisional excitation; the J=3–2 line detected by DGG97 (in an observation that could not have resolved it) requires  $n(\text{H}_2) > 10^6$  cm<sup>-3</sup>. Our maps show therefore that the gas density in the disk is high to radial distance  $> 2''$  (see also Sect. 4.2).

The integrated intensity data were fitted in the same way as the continuum data. The results are summarized in Table 1, and displayed in Fig. 5. In <sup>13</sup>CO, the ring and disk components can easily be distinguished, with the disk contributing to about 30% of the total flux. The limited angular resolution of the HCO<sup>+</sup> observations makes the fit less conclusive; we used the inner and outer ring radii measured from the continuum emission as fixed parameters to improve the determinations of the outer disk radius and of the relative flux densities of the ring and disk.

While our data can be perfectly fitted by a disk + ring model, we stress that they cannot be represented by a “standard” disk with a density power law and large inner radius. In DGS94, we showed that a surface density power law  $\Sigma(r) \propto r^{-p}$  with  $p = 1.5$  produces too extended continuum emission (DGS94, Fig. 6). Only extremely steep laws ( $p \simeq 5$ ) would avoid this problem, but they fail to produce sufficiently extended <sup>13</sup>CO and HCO<sup>+</sup> line emission. Furthermore, in Fig. 2, the zeros of the visibility function are *exactly equally spaced*: this property is reproduced by the Fourier transform of narrow rings, but not by that of truncated power laws with large ratio between the outer and inner radius.

## 4. Modelling

The simple analysis presented before clearly demonstrates that the gas and dust in the GG Tau system is distributed in two major components: a circumbinary ring or annulus, most easily detected by its 1.4 mm continuum emission, and an outer disk extending at least up to 700 AU, which is clearly visible in the <sup>13</sup>CO J=2–1 line.

### 4.1. Model description

Since the continuum data can be perfectly fitted by a uniform brightness ring with sharp edges (see Fig. 2), we assume that the close binary is surrounded by a circular ring of constant density, with a Gaussian profile at both edges ( $1/e$  width  $W_r$ , see Table 1), which is surrounded by a “standard” disk with power law distributions for density, temperature, velocity and scale height.

To determine more precisely the ring and disk parameters, we model all observed emission following a  $\chi^2$  minimization

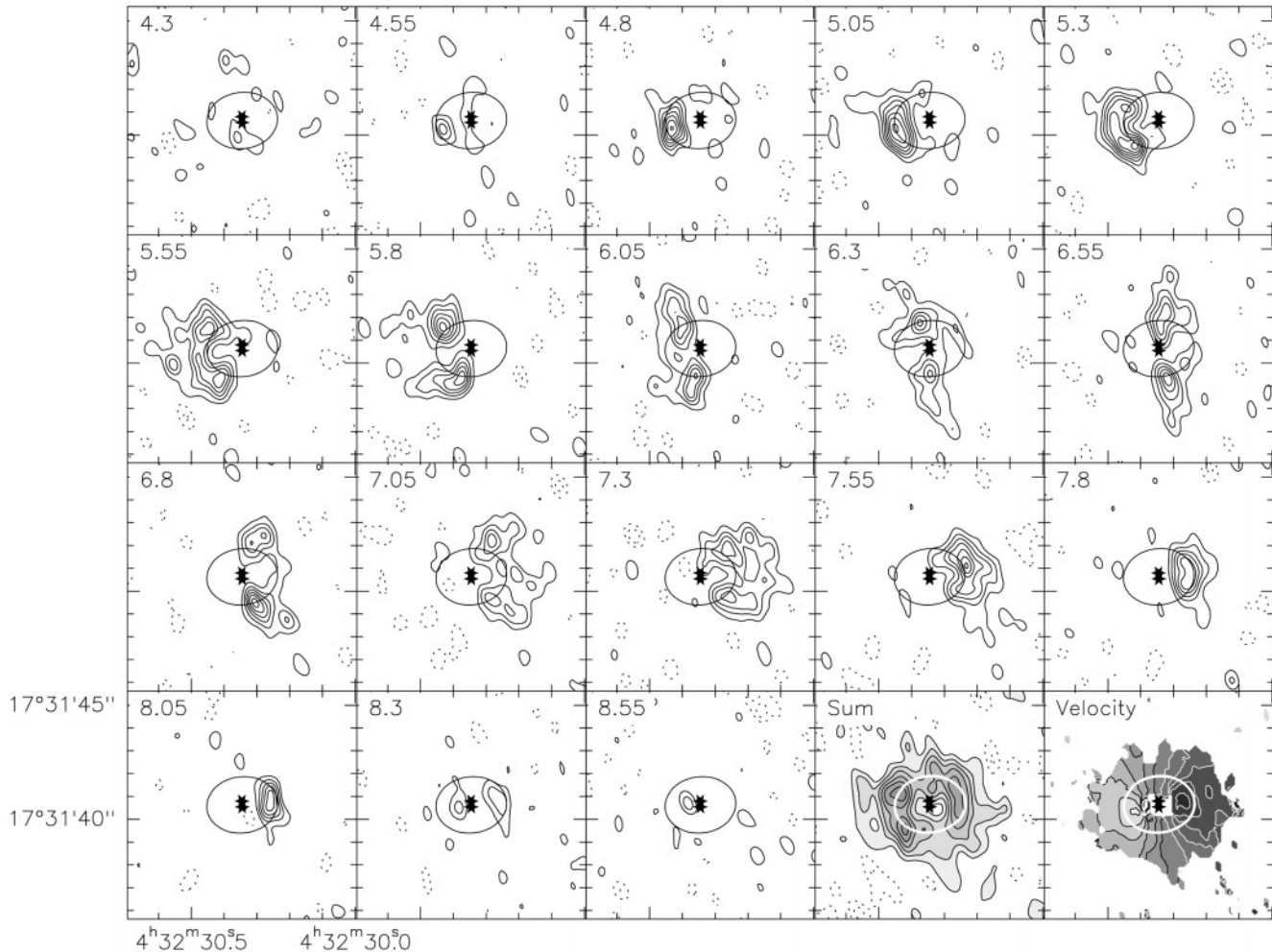


**Fig. 3.** Channel maps of the  $^{13}\text{CO}$  J=2–1 line emission in GG Tau. Contour spacing is 50 mJy/beam ( $2.5\text{ K}$ ,  $2\sigma$ ). The ellipse indicates the mean position of the continuum emission. The last two panels show maps of the velocity-integrated line intensity (contour spacing  $0.1\text{ Jy/beam km s}^{-1}$ ), and average velocity, in the sense of the intensity-weighted velocity (contour spacing  $0.3\text{ km s}^{-1}$ , starting at  $4.2\text{ km s}^{-1}$ ).

method similar to that described in Guilloteau & Dutrey (1998, GD98) for the single star DM Tau. The disk model corresponds to a non self gravitating disk (see Pringle 1981). Since the mass of the circumbinary disk is about  $1/10^{\text{th}}$  of the stellar mass, we cannot reject the possibility that self gravitation plays a significant role in the disk. Given the limitations of the current observations, we will neglect this possible complication.

Model parameters are described in Table 2. The orientation and disk inclination are constrained independently by the geometrical parameters of the elliptical projection of the ring, and by the velocity pattern of  $^{13}\text{CO}$  and  $\text{HCO}^+$  line emissions. All three determinations agree within the statistical errors. Because the existence of the ring brings a significant number of additional parameters to the model, a full  $\chi^2$  analysis could not be performed as in the case of DM Tau (GD98). Instead, the  $\chi^2$  analysis was performed on several sets of 2 or 3 coupled parameters, while fixing the other parameters to their best values. The error bars quoted in Table 2 are the statistical errors derived from these  $\chi^2$  analysis. Because this approach does not take into account all potential coupling between parameters, the

error bars on some of the parameters should be considered indicative. From the detailed analysis of parameter coupling performed by GD98, we estimate that realistic error bars have been determined for the kinematic parameters  $V_{\text{LSR}}$ ,  $V_{100}$ ,  $v$  and geometric parameters PA,  $i$ , because these are determined by the shape of the channel maps and are essentially independent on the assumed physical model. The ring geometric parameters ( $R_i$ ,  $R_o$ ,  $W_r$ ) are also well constrained, because the ring is so overdense as compared to the outer disk.

On the contrary, specific assumptions were made for the temperature and outer disk density laws. These assumptions are discussed in Sect. 4.2 and Sect. 4.4. The errors quoted in Table 2 for these parameters are only the statistical errors due to the thermal noise of the observations within the frame of these assumptions.

#### 4.2. Dust emission and $\text{H}_2$ densities

We assume a dust emissivity  $\kappa_\nu = 0.1(\nu/10^{12}\text{Hz})^\beta\text{ cm}^{-2}/\text{g}$  (see Beckwith et al., 1990). The dust spectral index  $\beta$  is

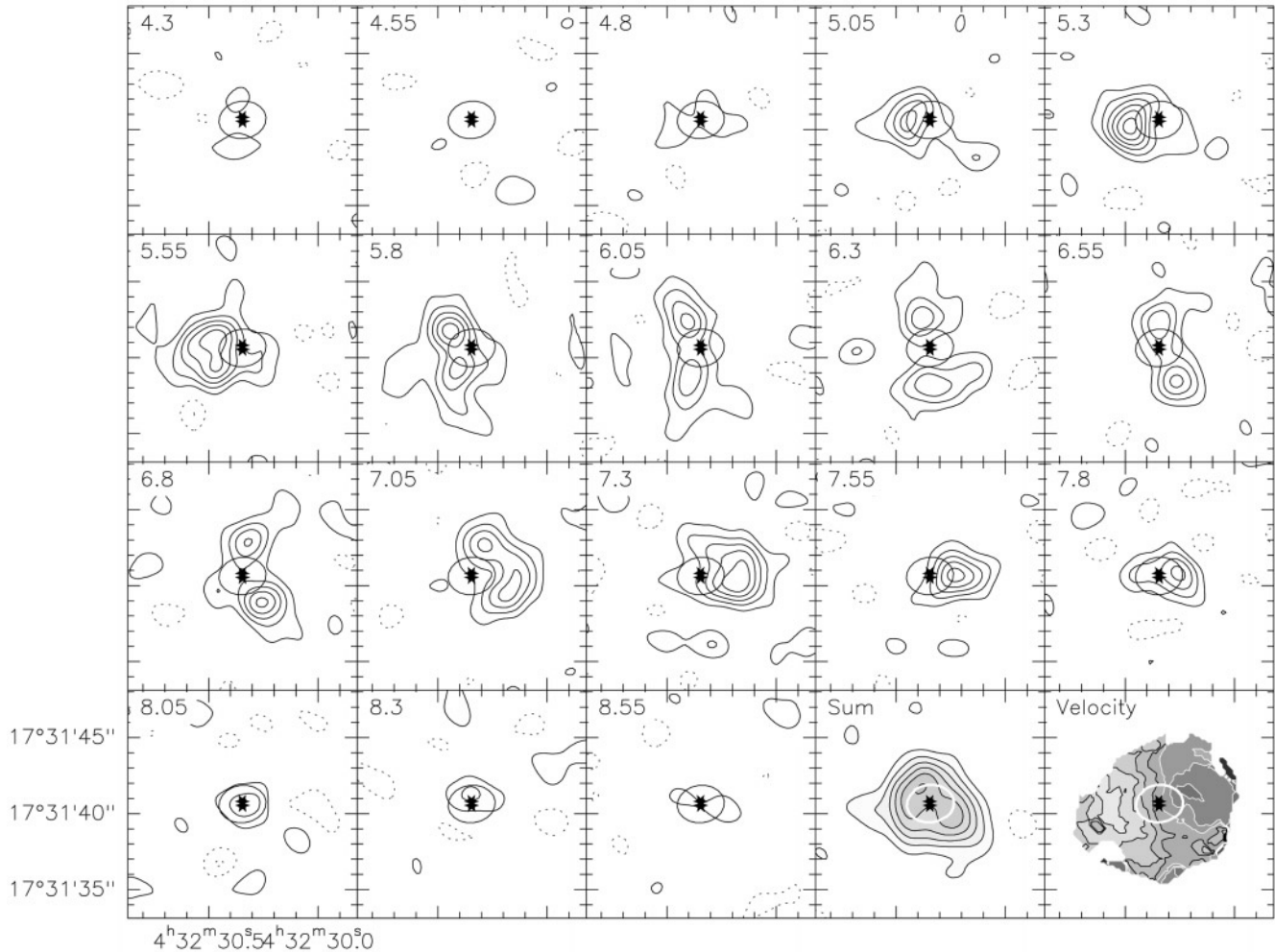


**Fig. 4.** Channel maps of  $\text{H}^{12}\text{CO}^+$   $J=1-0$  emission in the same format as Fig. 3. Here the synthesized beam is  $2.0 \times 2.0''$  and the contour spacing is 20 mJy/beam (or 0.77 K). The rms noise is 11 mJy/beam. The last two panels are maps of the velocity-integrated line intensity (contour spacing 0.05 Jy/beam  $\text{km s}^{-1}$ ), and average velocity ( $0.3 \text{ km s}^{-1}$  contour intervals starting at  $4.2 \text{ km s}^{-1}$ ).

constrained by the 1.4 mm, 3.4 mm and 2.7 mm continuum flux from DGS94. With the values given in Table 1, we find  $\beta = 1.15 \pm 0.10$ . Using the temperature derived from  $^{13}\text{CO}$   $J=2-1$  data (Sect. 3.2 and Sect. 4.4), and the dust emissivity as derived above, we find that a ring mid-plane density of  $1.6 \pm 0.1 \cdot 10^9 \text{ cm}^{-3}$  is required to reproduce the mm flux densities. The corresponding  $\text{H}_2$  surface density is  $\sim 1.4 \cdot 10^{24} \text{ cm}^{-2}$  in the ring, implying an optical depth across the ring of 0.11 at 1.4 mm. The total ring+disk mass is then  $0.12 M_{\odot}$ .

The sharpness of the inner edge of the dust *ring* is characterized by its  $1/e$  width,  $10 \pm 5 \text{ AU}$ . The *outer* ring edge is also very sharp. We note that the radial profile proposed by DGS94 does not reproduce adequately the new 1.4 mm continuum image, because the Gaussian profile assumed by DGS94 for the ring density law cannot represent this sharp *outer* ring edge seen in the new sub-arcsecond resolution image. All 3 continuum images are well fitted by the new model.

While the ring parameters are well determined, the best fit parameters for the density law in the *disk* are more uncertain, because of the limited dynamic range of the continuum image,

and because some continuum emission may originate between the GG Tau a and b systems. Densities higher than given in Table 2 would produce too much continuum flux from the disk, and can thus be safely excluded, but values lower by a factor 2 to 4 are acceptable. The exponent of the density law is also somewhat uncertain; very low values ( $< 2.5$ ) are excluded however, and the best fit is compatible with a surface density law  $\Sigma(r) = r^{-1.5}$ . Even accounting for a possible factor of 2–4, the disk mid-plane density of  $\sim 6 \cdot 10^7 \text{ cm}^{-3}$  at 300 AU is high enough to guarantee thermalization of the  $\text{HCO}^+$   $J=1-0$  line until a radius of more than 2000 AU, and that of the  $\text{HCO}^+$   $J=3-2$  line up to 600 AU.

With these values, the ring is 18 times denser than the disk at the disk–ring separation, but the outer disk still contains about 30% of the mass.

#### 4.3. Kinematics of the circumbinary disk

The high angular resolution and high signal to noise of the  $^{13}\text{CO}$   $J=2-1$  emission allows an accurate determination of the rotation

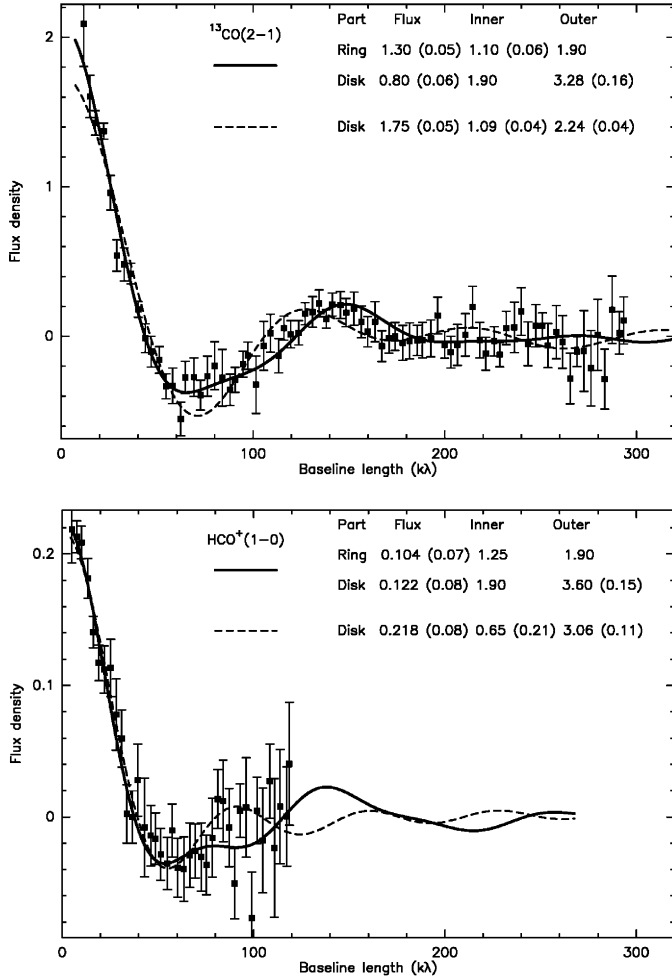


**Fig. 5.**  $u, v$ -plane visibilities for  $\text{HCO}^+$  and  $^{13}\text{CO}$ , plotted as the real part of the flux, as a function of circularised baseline length (in units of the wavelength) for the observed data (solid dots and  $\pm 1\sigma$  error bars), and the two component (ring plus extended disk, thick line) and single component (thin line) model described in Sect. 3.1. The  $uv$  coordinates were rotated and stretched along the  $v$  axis by  $\cos(37^\circ)$  to compensate for the inclination of the disk.

law. Assuming a power law dependence  $V(r) \propto r^{-v}$  for the velocity, the exponent is constrained to be  $0.5 \pm 0.1$ . This provides direct evidence for Keplerian rotation, confirming DGS94. Since the inclination is accurately measured, the mass of the binary can be derived from the Keplerian velocity; from the velocity law in Table 2, we derive  $M = (1.28 \pm 0.07)(D/140 \text{ pc})M_\odot$ . The uncertainty includes that in the determination of the inclination (see GD98).

The channel maps also permit an estimate of the turbulent component of the line width,  $\delta V_{\text{turb}}$ . We find from the  $\chi^2$  analysis  $\delta V_{\text{turb}} \leq 0.06 \text{ km s}^{-1}$ .

#### 4.4. Gas temperature

Since the  $^{13}\text{CO}$  J=2–1 emission is optically thick in the ring, the temperature in the ring is well determined, with an average value of 35 K. The temperature law in the disk is more difficult

**Table 2.** Parameter description for the GG Tau disk+ring model

Systemic velocity	$V_{\text{LSR}}$	$6.38 \pm 0.02$	$\text{km s}^{-1}$
Orientation	PA	$7 \pm 2$	$^\circ$
Inclination	$i$	$37 \pm 1$	$^\circ$
Ring density	$n_r$	$1.6 \pm 0.1$	$10^9 \text{ cm}^{-3}$
Ring inner radius	$R_i$	$180 \pm 5$	AU
Ring outer radius	$R_o$	$260 \pm 5$	AU
Ring edge width	$W_r$	$10 \pm 5$	AU
Disk outer radius	$R_{\text{out}}$	$\sim 800$	AU
Disk density law: $n(r) = n_{300} \left(\frac{r}{300 \text{ AU}}\right)^{-s}$			
$\text{H}_2$ density	$n_{300}$	$5.8$	$10^7 \text{ cm}^{-3}$
exponent	$s$	$2.75 \pm 0.15$	
Temperature law: $T(r) = T_{300} \left(\frac{r}{300 \text{ AU}}\right)^{-q}$			
Temperature	$T_{300}$	$20 \pm 1$	K
exponent	$q$	$0.9 \pm 0.1$	
Scale Height law: $H(r) = H_{300} \left(\frac{r}{300 \text{ AU}}\right)^h$			
at 300 AU	$H_{300}$	$55 \pm 5$	AU
exponent	$h$	$1.05 \pm 0.05$	
Velocity law: $V(r) = V_{100} \left(\frac{r}{100 \text{ AU}}\right)^{-v}$			
velocity at 100 AU	$V_{100}$	$3.4 \pm 0.1$	$\text{km s}^{-1}$
exponent	$v$	$0.5 \pm 0.1$	
turbulent velocity	$\delta V_{\text{turb}}$	$\sim 0.06$	$\text{km s}^{-1}$
$^{13}\text{CO}$ Abundance	$X(^{13}\text{CO})$	$\sim 5$	$10^{-8}$
$\text{HCO}^+$ Abundance	$X(\text{HCO}^+)$	$\sim 3$	$10^{-11}$
Dust exponent	$\beta$	$1.15 \pm 0.10$	

to estimate. The most significant constraint is that the  $^{13}\text{CO}$  J=2–1 line brightness in the disk is much lower than in the ring. This requires either significantly lower kinetic temperature in the disk, and/or optically thin emission in the disk. The latter can be due to either lower  $\text{H}_2$  densities, or lower  $^{13}\text{CO}$  abundance. The 3 parameters (temperature, density, abundance) are strongly coupled, and cannot be separated with this data set alone.

We propose in Table 2 a temperature law in the disk which is consistent with the kinetic temperature determined in the ring. This solution is not unique; however this is the solution with constant and maximal (with respect to the choice of temperature)  $^{13}\text{CO}$  abundance. Better determination can only be made by using an optically thick molecular tracer like  $^{12}\text{CO}$ .

We note that our results suggest that the kinetic temperature drops very quickly with distance from the star. Assuming a power law dependence, we find an exponent  $q \simeq 0.9$ . This is much steeper than in disks around single stars like DM Tau and GM Aur, where  $q \simeq 0.63$  (GD98, Dutrey et al. 1998). The ring geometry offers a natural explanation for this effect. Since the ring is highly optically thick in the infrared, the kinetic temperature is given to first order by

$$4\pi r^2 \sigma (T(r))^4 = L \cos(\gamma) \quad (1)$$

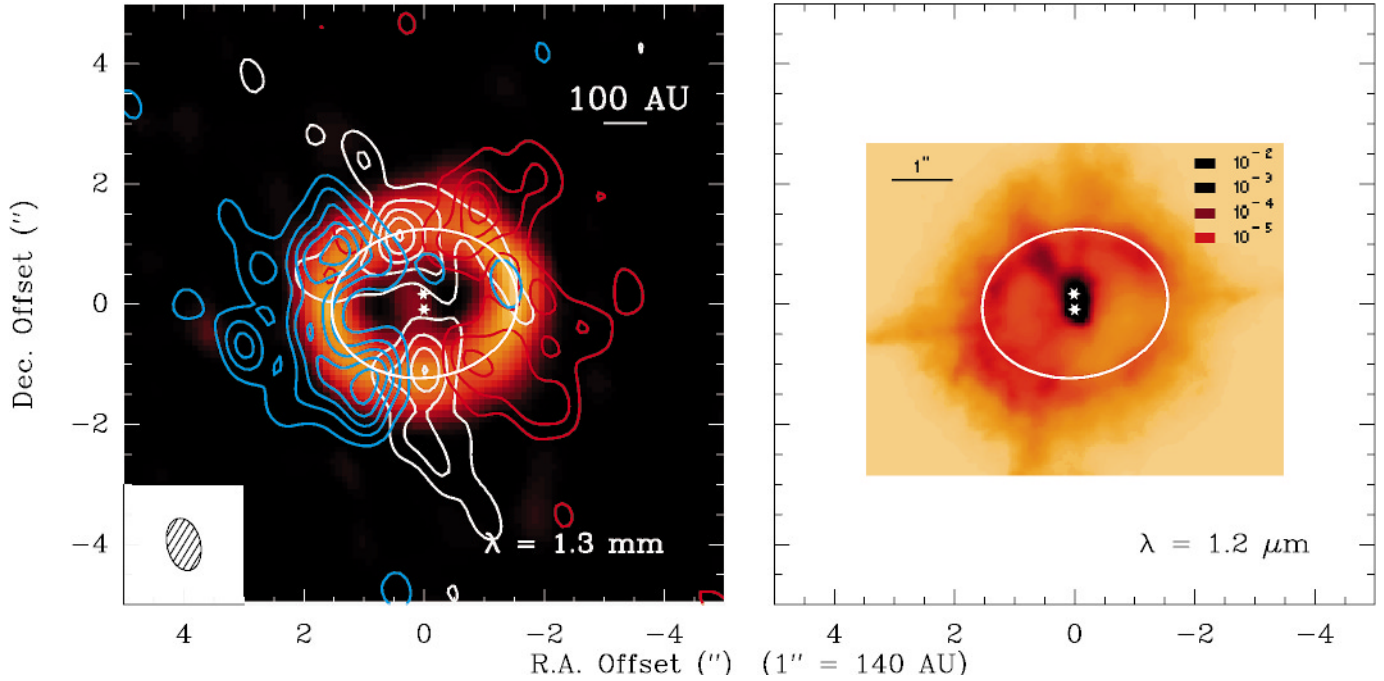


**Fig. 6a and b.** Comparison of the  $^{13}\text{CO}$  J=2–1 line emission at  $V = 5.55$  (blue contours),  $6.30$  (white contours) and  $7.05 \text{ km s}^{-1}$  (red contours), overlaid on a false colour image of the  $1.4 \text{ mm}$  continuum emission and **b** J-band emission resolved by RRNGJ. The white ellipse indicates the ring average radius.

where  $\sigma$  is the Stefan-Boltzmann constant,  $L$  the total (star + inner disks) luminosity, and  $\gamma$  the mean incidence angle of the radiation on the disk surface. As the effective geometric thickness of the ring (at  $\tau = 1$  in the near-IR) is large (120 AU, see Sect. 5.1),  $\cos(\gamma) \simeq 0.6$ . Strom et al. (1989) quote a luminosity  $L \sim 3L_{\odot}$ , including the IR excess, for the GG Tau A/a system. Hence, we find  $T(R_{\text{in}}) = T(180 \text{ AU}) = 34 \text{ K}$ , in good agreement with our measurement. Similarly, for the outer disk, heating occurs mostly through the disk surface and  $\cos(\gamma) \simeq H(r)/r \simeq 0.2$ . We thus find  $T(300 \text{ AU}) = 20 \text{ K}$ .

#### 4.5. Molecular abundances

Even inside the disk, the density law derived from the dust emission is high enough to thermalize the  $\text{HCO}^+$  J=1–0 line, and a fortiori the  $^{13}\text{CO}$  J=2–1 line. If the line emission is optically thin, we can then estimate the abundance. With the above temperature and density laws, and assuming that the molecular abundances are uniform throughout the circumbinary disk, we find molecular abundances  $X(^{13}\text{CO}) = 5 \cdot 10^{-8}$ , and  $X(\text{HCO}^+) = 4 \cdot 10^{-11}$ , corresponding to depletions (relative to the Taurus “standard” abundances of  $10^{-6}$  and  $8 \cdot 10^{-9}$  respectively, Ohishi et al. 1992) of  $\simeq 20$  for  $^{13}\text{CO}$  (in perfect agreement with DGS94) and  $\simeq 200$  for  $\text{HCO}^+$ . The latter is much larger than the value of  $\sim 10$  found by DGG97 for DM Tau. Since the density in the disk is most likely an upper limit (because of uncertainty in the disk continuum emission, see Sect. 4.2), and

since all observed spectral lines are highly optically thick in the ring, the actual depletions may be  $\simeq 2$  to 4 times lower.

For  $\text{HCO}^+$  J=1–0, a slightly better model (at the  $4\sigma$  level) is obtained with different abundances in the ring and in the disk with  $X_{\text{ring}}(\text{HCO}^+) = 2.0 \cdot 10^{-11}$   $X_{\text{disk}}(\text{HCO}^+) = 4.5 \cdot 10^{-11}$ , corresponding to depletions of 400 and 180 respectively. Although the significance of this result is questionable, it suggests that  $\text{HCO}^+$  could be more severely depleted in the densest regions.

## 5. Discussion

### 5.1. Geometrical thickness of the circumbinary ring

RRNGJ observed orbital motion of the stars in the close binary in the clockwise sense. The spectral line images show that the velocity of the eastern side of the disk is toward us, and on the western side, away from us. Assuming that the orbital angular momenta of the stars and disk are roughly in the same direction, this means that the disk is inclined such that its northern edge is nearest to us. Fig. 6 compares the current data with RRNGJ’s J band image. The relative brightness of the northern and southern portions of the disk at J are determined by the phase function of the dust. The brighter northern part indicates that forward scattering is favored, as discussed by RRNGJ.

The J band and  $1.4 \text{ mm}$  images have been registered using the fact that the binary center of mass must lie at the center of the dust ring, under the assumption that the ring is intrinsically circular. To define the center of mass, we used a mass

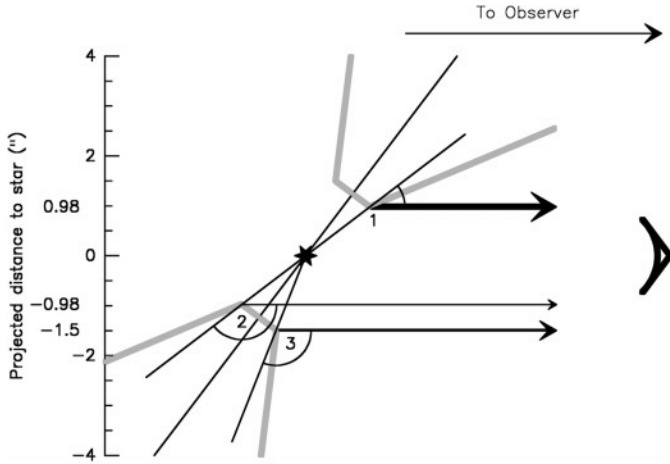


**Fig. 7.** Shift of the apparent inner edges of an inclined thick flared disk in scattered light. The thick grey lines indicate the disk edges. The arrow size and line thickness indicate the relative intensity of scattered rays from the 3 visible inner edges of the disk (1, 2 and 3). Because of the larger scattering angle required for the farthest part (point 2), the inner boundary appears brighter and closer to the illuminating stars for the closest part of thick disk (point 1 versus point 3).

ratio of 1:2 for the binary; assuming a mass ratio of 1:1 would shift northward the center of mass by  $0.04''$ , slightly increasing the effect mentioned below. With this accurate registration, the ring seen in scattered light at  $1.2 \mu\text{m}$  is obviously shifted from the ring position determined from the 1.4 mm continuum emission. Such a situation can be easily explained if the ring is not geometrically thin, and because the phase function of the dust favors forward scattering at  $1.2 \mu\text{m}$ . In this case, the inner edge of the ring which is closest to the observer (i.e. the northern one in our case) appears shifted inwards in the IR image by  $\approx h/2\sin(i)$  where  $h$  is the ring thickness (see Fig. 7). No shift is observed at 1.4 mm because the dust emission is optically thin. The measured shift, about  $0.25''$ , indicates a ring thickness  $t \simeq 120 \text{ AU}$  at the inner ring edge ( $r = 180 \text{ AU}$ ). Although such a value looks *a priori* very large as compared to the ring inner radius, it compares well with the scale height derived from the models presented in Sect. 4. Assuming a NIR optical depth of 100, the ring becomes optically thick along the  $z$  direction at  $z = 1.65H$ , so that the apparent thickness of the disk in the NIR is  $t = 3.3H$ . With a scale height  $H = 32 \text{ AU}$  at the inner edge of the ring (derived from Table 2), we find  $t = 106 \text{ AU}$ .

Although the above effect accounts for the apparent shift between the optically visible ring and the stars, with this image registration the binary appears slightly shifted from the weak 1.4 mm dust emission which is presumably tracing the inner (circumstellar) disks (see Fig. 1). The effect is marginal, given the low signal to noise ratio of the 1.4 mm data, but it suggests that the ring might be slightly elliptical, with the center of mass located at one of the ellipse foci, closer to the Eastern edge of the ring. Note that, as shown by RRNGJ, only a very small ellipticity of the ring is required to produce a significant shift of the center of mass from the ring geometrical center.

Note also that in continuum, the Western part of the ring is brighter than the Eastern part. The effect is more pronounced in the continuum at 3.4 mm and 2.7 mm (DGS94), not significant at 1.4 mm, and not detectable in the line maps. This suggests this effect may be due to a column density enhancement, which is only detectable with the most optically thin tracers.

## 5.2. Circumstellar disk emission

At the location of the binary, we detect at 1.4 mm about 10 mJy which is likely coming from one or two inner circumstellar disks. This emission may arise from thermal dust or free-free emission from compact ionised jets. An upper limit of  $\sim 2\text{--}3 \text{ mJy}$  is obtained for the flux at 3.4 mm in the direction of the binary (see Fig. 1), consistent with a spectral index  $\sim 2$  or higher (although the error bars are large). In the absence of detection at other wavelengths, we thus assume that the 1.4 mm continuum emission is due to thermal dust associated to two disks radiating equal flux ( $\sim 5 \text{ mJy}$ ). Assuming a uniform temperature of  $T_k = 100 \text{ K}$  as representative of the whole disk (based on the extrapolation of the temperature law of Table 2), we find a lower limit on the mass of  $\sim 0.8 \cdot 10^{-4} M_\odot$  and a lower limit on the radius of  $\sim 4 \text{ AU}$  (see Dutrey et al. 1996). Note that such a small radius is in agreement with the tidal truncation which roughly implies that inner disks cannot be larger than  $\sim 20 \text{ AU}$  (i.e.  $1/3^{\text{rd}}$  of the semi-major axis of the binary orbit).

## 5.3. Mass of the binary

The measured rotation velocity implies a mass  $M = 1.28 \pm 0.07 M_\odot$  for the assumed distance of 140 pc. This is comparable to (although slightly lower than) the  $M \simeq 1.6 M_\odot$  derived by RRNGJ from the orbital motions of the binary. Note that our mass estimate scales linearly with the assumed distance  $D$ , while the mass derived by RRNGJ scales as  $D^3$ .

## 6. Summary

The circumbinary disk surrounded GG Tau has been simultaneously imaged at resolution of  $\sim 0.6 \times 0.9''$  by the IRAM interferometer in  $^{13}\text{CO}$  J=2–1 and continuum at 1.4 mm, and at a resolution of  $\sim 2''$  in  $\text{HCO}^+$  J=1–0 and continuum at 3.4 mm. These observations confirm the previous observations and model by DGS94 but also allow a more detailed analysis of the ring and disk structure. Among them, the most important results are:

- The circumbinary disk has two components: a narrow ring with sharp edges (corresponding to 90% of the 1.4 mm flux or 70% of the mass) and an extended disk (up to  $R_{\text{out}} \simeq 800 \text{ AU}$ ). The extended disk is mainly detected in  $^{13}\text{CO}$  and  $\text{HCO}^+$ . The total disk+ring mass is about  $0.12 M_\odot$ .
- The ring has sharp inner and outer edges ( $W_r \leq 10 \text{ AU}$ ) and its geometrical width is  $\sim 80 \pm 5 \text{ AU}$ .
- Circumstellar 1.4 mm emission is also detected, and is consistent with tidally truncated circumstellar disks of radius  $R \sim 4\text{--}20 \text{ AU}$  and total mass  $\geq 1.5 \cdot 10^{-4} M_\odot$ .

- The apparent shift between the optical and radio rings is consistent with a scale height of 30 AU (at the inner edge of the disk) and an optical depth of  $\sim 100$  in the near IR, as extrapolated from the millimeter range.
- The kinetic temperature profile is consistent with heating by the star and inner disks radiation. In particular, the ring is much warmer than the outer disk.
- The dynamical mass of the system is accurately determined  $1.28 \pm 0.07(D/140\text{pc})M_{\odot}$ .

Given that the circumbinary material is dominated by the dusty ring, we propose to nickname GG Tau “The Ring World”.

*Acknowledgements.* We thank Claude and François Roddier for providing us the IR image of GG Tau. We thank Larry Niven for the nickname of GG Tau.

## References

- Beckwith S.V.W., Sargent A.I., Chini R.S., Güsten R., 1990, AJ 99, 924
- Dutrey A., Guilloteau S., Simon M., 1994, A&A 286, 149 (DGS94)
- Dutrey A., Guilloteau S., Duvert G., et al., 1996, A&A 309, 493
- Dutrey A., Guilloteau S., Guélin M., 1997, A&A 317, L55 (DGG97)
- Dutrey A., Guilloteau S., Prato L., et al., 1998, A&A 338, L63
- Elias J.H., 1978, ApJ 224, 857
- Guilloteau S., Delannoy J., Downes D., et al., 1992, A&A 262, 624
- Guilloteau S., Dutrey A., 1998, A&A 339, 467 (GD98)
- Herbig G., Bell K.R., 1988, Lick Obs. Bull. No. 1111
- Leinert Ch., Zinnecker H., Weitzel N., et al., 1993, A&A 278, 129
- Ohishi M., Irvine W.M., Kaifu N., 1992, Proc. IAU Symp. 150, p. 171
- Pringle J.E., 1981, ARA&A 19, 137
- Roddier C., Roddier F., Northcott J.E., Graves J.E., Jim K., 1996, ApJ 463, 326 (RRNGJ)
- Strom K.E., Strom S.E., Edwards S., Cabrit S., Skrutskie M.F., 1989, AJ 97, 1451